An estimation of Titan fluid and sediment properties based on sediment transport theory

Mike Ream

GEOL 394

Advisor: Karen Prestegaard

ABSTRACT:

Titan is the only other planetary body in the Solar System besides Earth known to currently support active fluvial processes. The Huygens Lander returned photographic evidence of fluvial activity, such as branching, sediment-filled channels. The sediment at the landing site consists of rounded cobbles strewn over a bed of finer-grained material which probably contained methane moisture in its pore spaces. The bimodal sediment size distribution observed at the Huygens lander site suggests simultaneous transport and deposition by two different mechanisms, such as bedload and suspended load. Although methane and ethane are the dominant components of Titan's surface fluid, they are not likely to be the sole constituent of the fluid, and a mixture of methane, ethane, and heavier hydrocarbons is much more likely. The composition of the sedimentary material is likewise poorly constrained. Application of known principles of sediment transport mechanics as derived from Earth systems is therefore made complicated by a wider possible range of sediment and fluid properties. This analysis uses a Metropolis Algorithm-based Monte Carlo method to constrain the densities of the sediment and fluid, as well as the viscosity of the fluid, from the bimodal grain size distribution observed at the landing site. The analysis was only partially successful, providing reliable constraints on the sediment density at a modal value of 735 kg/m^3, less reliable constraints on the fluid density of approximately 500-550 kg/m^3, and no constraints at all on the fluid viscosity. This is most likely due to changes in the density and viscosity of a sediment-laden fluid as it deposits its sediment load.

INTRODUCTION:

Numerous observations have been made of fluvial processes on Titan, Saturn's largest moon. Titan was discovered by Dutch astronomer Christiaan Huygens in 1655 in an early attempt to characterize Saturn's rings. Methane was first discovered in Titan's atmosphere by Kuiper in 1944. Like Earth, Titan's environmental conditions are near the triple point of a volatile substance, though in the case of Titan, the volatile is predominantly methane, not water. Earth-based spectral data indicate that a permanent opaque haze of methane aerosol is present in Titan's atmosphere, prompting widespread speculation of the presence of liquid methane, though whether this methane was able to precipitate from the atmosphere and form flowing or standing bodies on the surface remained unknown for lack of images. The Cassini-Huygens mission, a joint undertaking by NASA and ESA to further explore the Saturn system, is the source of all images to date of Titan's surface and has shown that such standing liquid bodies do indeed exist on the surface.

Evidence for a hydrological cycle:

Despite the fact that the dominant fluid is methane and not water, I will still employ the term "hydrological" to refer to Titan's volatile cycling processes in order to avoid potentially inaccurate terminology referring specifically to methane, such as "methanological", or awkward attempts to encompass all volatiles, such as "volatilological". Voyager observations show that Titan's atmosphere is approximately 98% nitrogen, with the remainder composed of methane, ethane, nitriles, acetylene, and complex hydrocarbons (Owen 1982). The atmospheric mole fraction of methane near the surface is 5 ± 1% (Tomasko et al. 2005). At an atmospheric pressure of 1467.6 mbar and a temperature of 93.8 K, the

relative hydrocarbon humidity is 50% (Tomasko et al 2005). Large storms in Titan's atmosphere have been observed by Cassini, which has been in orbit around Saturn for roughly 1/3 of a Saturnian year, or from late summer in the southern hemisphere to early spring in the northern hemisphere (Turtle et al 2011). Two large storm events, each between 1000 and 2000 km across and lasting several weeks, have been observed in the equatorial regions as of 2011, producing temporary changes in radar reflectivity of the surface over areas of ~$5e^{-5}$ km^2 (Turtle et al. 2011). The persistence of radar darkening after the storm event indicates possible prolonged wetting of the surface, such as pooling caused by a delay in drainage (Turtle et al. 2011) conducive to dissipation by fluvial processes. Perron et al. 2006 estimated a rainfall rate of 0.5 – 15 mm/hr over a period of at least two hours as the minimum required to transport sediment, but estimates of the possible intervals between erosive events is still poorly constrained, ranging from daily to several years.

Cassini SAR swaths have revealed widespread, extensive fluvial landforms, which originate in crenulated, generally radar-bright terrain and drain into radar-dark lakes, especially in the polar regions. Extensive networks, reaching several hundred kilometers in length, have been resolved by Cassini's SAR (Burr et al. 2012). These landforms exhibit a variety of different morphologies and radar reflectivities even at the low resolution (typically 1 km per pixel) of the SAR (Burr et al, 2012). Large lakes, some of them hundreds of km across, are found in both polar regions. Other landforms, thought to be dry lakebeds due to the similar morphology of their borders to the presently-filled lakes, have also been observed in Titan's equatorial regions.

Evidence for fluvial processes:

The Cassini mission also included the Huygens lander, a descent module intended to gather data on Titan's surface and atmosphere. It landed in Titan's equatorial region at latitude $10.2^o \pm 0.1^o$ S, longitude $167.6^o \pm 0.1^o$, which was subsequently covered by Cassini SAR swath T8 (Keller et al. 2008). See figure 3 for an aerial view of the landing site. Huygens's DISR (an abbreviation of Descent Imager, Spectral Radiometer) was equipped with three small lens telescopes called the High Resolution Imager (HLI), the Medium Resolution Imager (MRI), and the Side-Looking Imager (SLI). These imagers collectively cover a range of 8.3^o to 96^o from the nadir (Keller et al. 2008), with the HRI oriented closest to nadir, and the SLI oriented horizontally. During its descent, Huygens took a total of 1134 visible-light images, mostly with the HRI and MRI, of which only 580 were returned to Earth due to the failure of a transmission channel (Keller et al. 2008). The dense aerosol haze in the atmosphere prevented useful optical imaging of the surface above an altitude of ~40 km (Soderblom et al. 2007). Huygens captured 240 images below this altitude, which were later used to construct mosaics, such as figure 1, and which were used to stereographically determine the topography of two regions within 20 km north and east of the landing site (Tomasko et al. 2005; Soderblom et al. 2007).

The photographs show a dark, low-lying area between lighter areas with higher albedo. While topographic data is only available for a small portion of the lighter area, the part of the lighter area for which topography is known indicates that it is higher in elevation by 50 - 200 m (Soderblom et al. 2007). There are bright streak-like features parallel to the bright/dark boundary which may be drift deposits of bright material, further suggestive of fluid flow, or which may also be due to faulting (Tomasko et al.

2005). The terrain is overall quite convoluted – slopes are commonly 30° or even steeper, which approaches the angle of repose for unconsolidated material (Tomasko et al. 2005). The final set of images taken before landing, at an altitude of 200-300 m, do not show any boulders with sizes on the order of 1 m, despite sufficient resolution (Tomasko et al. 2005).

The optically dark areas have infrared spectral properties which are consistent with water ice mixed with impurities. The bright regions, on the other hand, have lower concentrations of water ice, and are probably mantled with aerosol dust precipitated from the atmosphere (Soderblom et al. 2007).

The darker region is fed by tributaries of two apparently distinct morphologies, shown in figure 1.

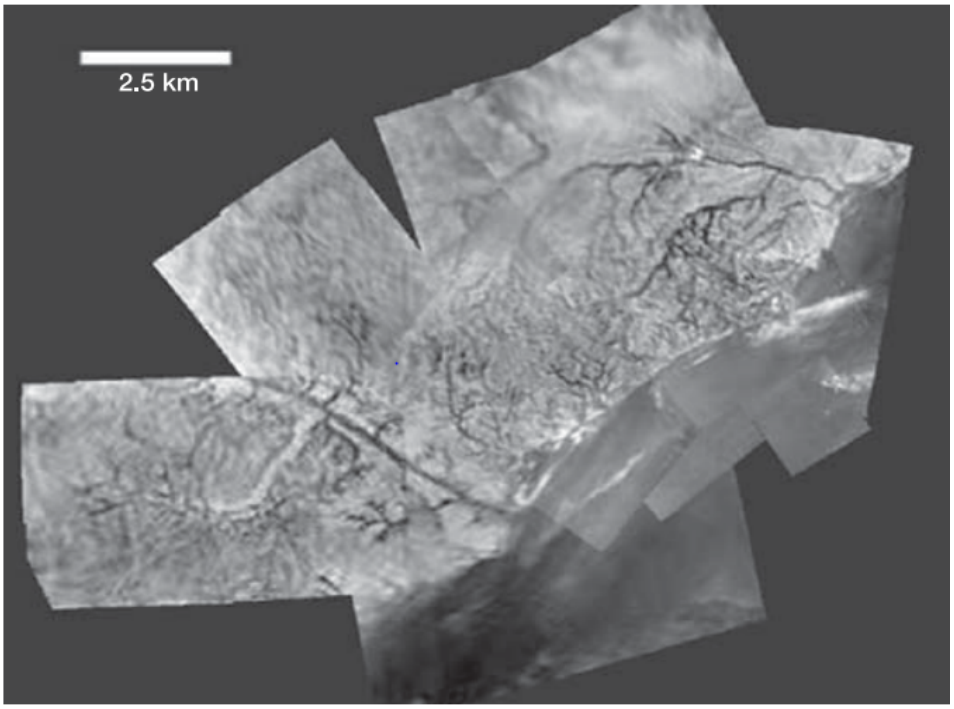

Figure 1. A mosaic image of Titan's surface as seen from 6.5 km altitude, showing fluvial networks draining into a darker region which itself displays flow features. North is up. The rectilinear network is on the western (left-hand) side of the image, the dendritic networks are to the east.

One of these tributaries has a mostly straight main stem, possibly tectonically controlled, with short lower-order branches feeding it at right angles. Such a rectilinear morphology is indicative of spring-fed channels or sapping erosion on Earth (Tomasko et al. 2005). Tectonic influences on network morphology have been proposed to account for networks elsewhere on Titan (Burr et al. 2013). The other networks, separated from the first network by a topographic divide (Soderblom et al. 2007), show a dendritic form distinct from their neighbor, suggestive of a distributed source such as liquid precipitation (Tomasko et al. 2005; Perron et al 2006). The region containing these networks is one of those for which topographic data is available. Topographic data indicate that the dendritic area is elevated with respect to the darker plain of the landing site by 50 m to 200 m. One of the main channels in this network is roughly 27 m deep and 100 m wide (Keller et al. 2008). These networks are far too small to be the sole source of material to the darker region (Tomasko et al. 2005). None of the finer features seen in these images are resolvable by Cassini's SAR.

The second region with mapped topography lies in the darker, lower area. Bright ridges, presumably made of the same material as that of the incised bright area mentioned above, protrude approximately 100 m above the bed and are associated with flow features (Soderblom et al. 2007).

Figure 2. Titan's surface as seen by Huygens after landing. Note the possible flow features - darker streaks originating from some of the rocks in the center-left of the picture and extending to the right. The elongated cobble on the bottom left of the image is ~20 cm long. The view faces to the south (Tomasko et al. 2005).

Sedimentary characteristics at the landing site:

After landing, Huygens continued to take photographs, though because it was no longer rotating, it obtained the same image, figure 2, with the MRI and SLI 223 times until its power supply was exhausted (Soderblom et al. 2007). The terrain is completely covered by rounded cobbles overlying finer-grained material. These sediments were therefore emplaced by processes which segregate grains by their size (Tomasko et al. 2005). The majority of the surface at the landing site is covered by rocks larger than 5 cm in diameter (Tomasko et al. 2005; Keller et al. 2008). Dark features extending from some of the rocks may be a result of flow (Tomasko et al. 2005), which, considering that the DISR imagers faced south after landing, would imply that the flow direction is from WNW to ESE (Soderblom et al. 2007). This is parallel to the elevated bright-dark boundary, which may be a channel bank, seen in figure 3 (Soderblom et al. 2007). The maximum resolution of these images is in MRI's closest foreground, at 3 mm per pixel (Tomasko et al. 2005).

Although the precise composition of the rocks is uncertain, infrared spectral observations made from Earth and from Cassini strongly suggest that water ice is a major component of Titan's surface, but this water ice is mixed with organic compounds of a largely unknown composition, producing a spectral signature that is thus far unique in the Solar System (Tomasko et al. 2005). Titan also has a rather low bulk density, consistent with a crust which is made principally of water ice (Perron et al. 2006).

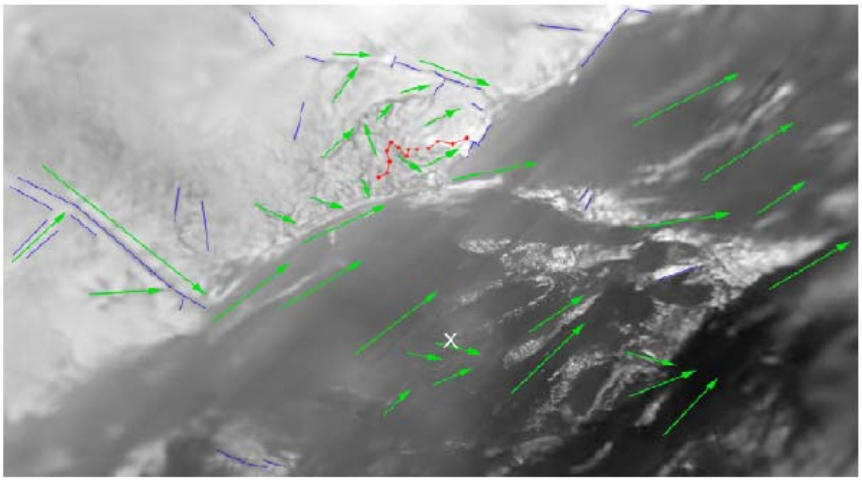

Figure 3. A 18.3X10.9 km photomosaic showing the Huygens landing site (white X), inferred flow directions (green arrows), tectonic features (blue lines), and a drainage divide (red lines).

The Huygens lander included as part of its Surface Science Package an instrument known as a penetrometer, meant to provide information about the mechanical properties of the regolith in the event of a solid-surface landing. The penetrometer data were interpreted by comparison to subsequent experimental results on a variety of granular materials using a replica penetrometer. This experimentation showed that the surface consists of a weak uppermost layer, perhaps aerosol dust, about 7 mm thick, with a texture somewhat like that of terrestrial snow (Atkinson et al. 2010). Underneath this layer was either a rigid crust suggestive either of an evaporite, or a grain of larger material being pushed out of the way by the lander as it settled into the soil (Atkinson et al. 2010). Below this obstruction was an underlying granular material with a mean grain size of ~2 mm (Atkinson et al. 2010). See figure 4. Additionally, an onboard Gas Chromatograph Mass Spectrometer detected a rise in the ambient methane vapor mole fraction within a few minutes after landing, indicative of evaporation of methane moisture present in the pore spaces of the soil, perhaps as a result of the heat generated by the lander's 20 Watt surface science lamp (Atkinson et al. 2010).

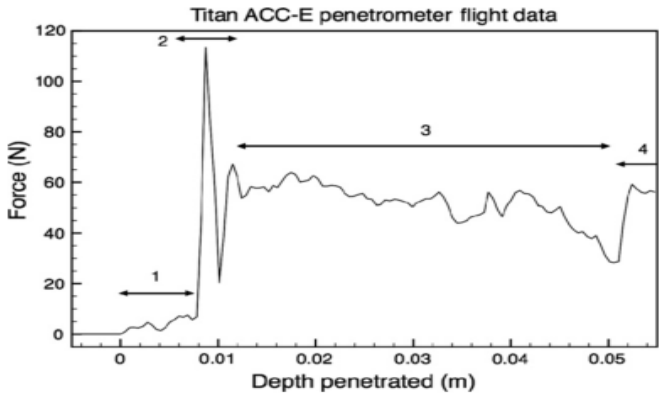

Figure 4. A plot of resisting force vs. depth penetrated for the Huygens Lander's penetrometer. From Atkinson et al. 2010.

All of these surface characteristics support the inference that the landing site is near or in a channel, and is covered by sedimentary material of two different mean grain sizes. A close Earth analogue to this environment could be an ephemeral braided channel in a desert. If physical sediment transport processes on Earth are fundamentally the same as those on Titan, then these granular materials are representative of deposition in a fluvial environment, and the roundness of the grains is the result of abrasion in transport. The area in the mid-ground which is clear of larger-sized material may have been the path of

the last liquid outwash. It is reasonable to assume that a similar grain size distribution as that observed in the SLI (Side-Looking imager) image foreground probably occupied that area as well.

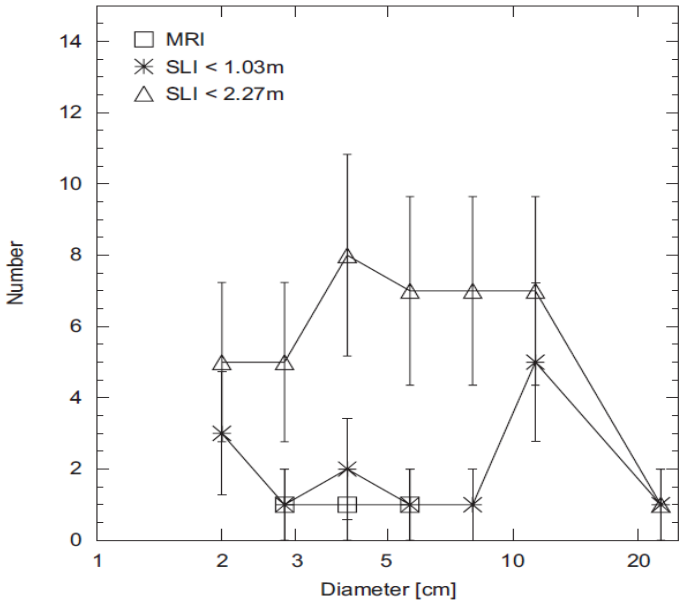

Figure 6. The size-number distribution measured by Keller et al. 2008.

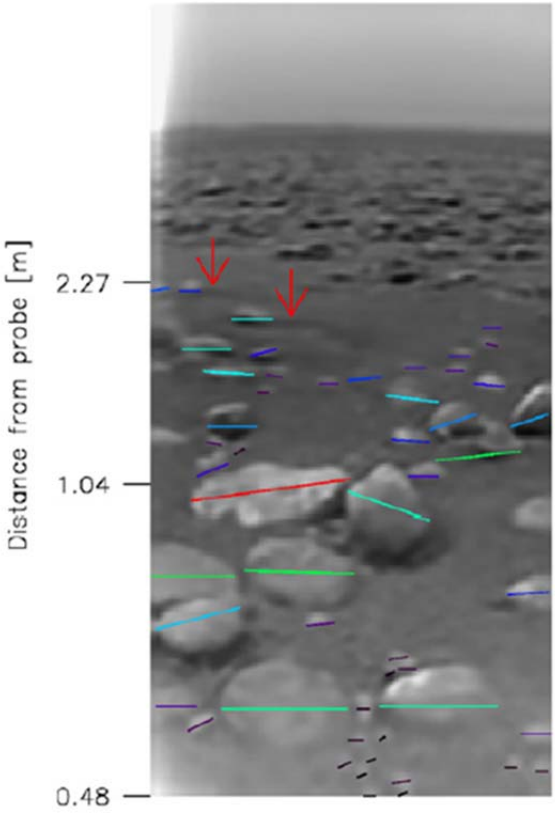

Figure 5. Most of the 56 measured grains are from this SLI image. The arrows point to flow features which point in the downstream direction. The colored lines represent increasing size, from purple to red.

PROBLEM TO BE SOLVED:

There is an apparent bimodality in the grain size distribution between the data returned by the penetrometer and the data extrapolated from the images, shown in figure 6. The largest grain size of ~20 cm (Keller et al. 2008) suggests an upper limit of the capacity of the flow in the channel to transport sediment (Tomasko et al. 2005). The mean size of the smaller size fraction likewise suggests an upper limit on the capacity of the flow to carry sediment in suspension. The focus of this project is to determine: 1) which transport process or combination of transport processes capable of producing a bimodal size distribution deposited this material; and 2) to determine whether the compositions of the sediment or the fluid can be constrained by sediment transport theory.

Relevant sediment transport mechanics:

Sediment can be transported by being dragged, bounced, or rolled along the bed; or by suspension in a turbulent flow of wind or water. An underlying assumption behind this paper is that these processes are universal, regardless of the planet on which they occur.

Bedload transport occurs when the flow first initiates motion of grains across the bed. The average boundary shear stress of a fluid in an open channel is described by the du Boys equation:

$$\tau = \rho g d S$$

where τ is the shear stress, ρ is the density of the fluid, d is the depth of the flow, g is gravitational acceleration (in the case of Titan, g = 1.35 m/s^2, or about 14% that of Earth), and S is either the slope over which the fluid flows, or the slope of the liquid itself. *Critical shear stress* is defined as the amount of shear stress required for the onset of grain motion. Shear stress increases as a result of an increase in precipitation or runoff, because this adds to the depth of flow in the drainage channels. When flow shear stresses are enough to dislodge a grain from the bed, but not enough to fully suspend the grain into the flow, the grains begin to roll and bounce along the bed in the direction of flow. These two modes of grain motion are collectively known as bedload. Bedload is generally the first transport mode to initiate as shear stresses increase due to increasing depth during a discharge event.

If bedload transport of larger material, such as the material seen in Figure 5, can occur in a channel, then conditions may also allow for suspended load transport of the smaller material. Suspension is another transport mode, associated with higher turbulence, in which the moving grains make very little or no contact with the bed, traveling in the fluid column at some height above the bed. The transition between saltation and suspension does not have a sharp boundary - grains can become suspended for a short period of time before falling back towards the bed. Whether the grain enters into suspension is primarily controlled by its settling velocity, which is itself controlled by the upward drag forces on it are equal to the downward force of gravity. When the settling velocity is exceeded by the shear velocity (a quantity used to evaluate turbulence, defined below), the shear stresses of the flow at that height above the bed exceed the pull of gravity, and the bed particles are prevented from falling.

If two distinct grain sizes are simultaneously transported by a flow, then there are likely either two different processes acting to transport the material, or two different material densities. Shear stress decreases with further distance downstream because slope decreases more rapidly than depth increases. Therefore, the shear velocity will decrease downstream as well, and when it has decreased to a value equal to the fall velocity of the particle, the particle will move back into bedload and (if flow continues to decrease) be deposited on the streambed. Given the apparently ephemeral nature of discharge events at the Huygens landing site, reduction in flow depth due to exhaustion of fluid supply may happen quickly, and is probably what dictates the cessation of grain motion. As the depth, and therefore the shear stress, decreases, the coarser fraction of the suspended material transitions back to bedload first, moving as a layer of sand onto the bed. This new layer of sand moving along the bed makes the bed smoother, decreasing the critical dimensionless shear stress (defined below), increasing the mobility of the coarse bedload fraction. As the flow depth decreases yet further, the shear stress decreases below its critical value, and bedload transport slows to a halt as well, leaving the cobbles strewn on top of the finer material, resulting in the well-known “gravel over sand” bed morphology observed on Earth.

Critical dimensionless shear stress:

The use of non-dimensional parameters is important in geomorphology in order to provide scaling relationships between different phenomena. A quantity widely used to describe the initiation of motion of sediment particles flowing liquid on the bed of a channel is the critical dimensionless shear stress, also known as the Shields number, which is the ratio of fluid shear forces to the resistance forces of the grains:

$$\tau_{*crit} = \frac{\rho g d S}{(\sigma - \rho) g D} = \frac{fluid\ shear\ stress}{grain\ resisting\ forces}$$

where ρ = density of the fluid, g = gravitational acceleration, d = flow depth, S = bed slope, σ = density of the sediment material, and D = diameter of the sediment particle. Shields experimentally determined that, for homogeneous sand beds, critical dimensionless shear stress does not appreciably increase beyond a value of ~0.06 for grains larger than about 0.5 cm. When the forces holding the grain in place are exceeded by the shear forces of the flow, the grain begins to move, and bedload transport has been initiated.

A natural stream bed, of course, does not have a perfectly homogeneous grain size, nor is the bed perfectly non-cohesive. The principal factors which cause τ_{*crit} to vary are surface roughness, bed cohesion, and sand-gravel interactions, described below.

The roughness coefficient, k_s, is a measure of the protrusions of the sediment grains above the bed, and is an important factor governing the flow conditions at and directly above the bed, which in turn influence the amount and mode of entrainment. It is especially relevant in the case of heterogeneous beds, but plays a role in homogeneous sediments as well. Wiberg and Smith 1987 used a first-principle approach based on the balance of forces on individual sediment grains to derive a mathematical expression describing the motion of sediments in mixed-size beds. Stream beds with heterogeneous particle size mixtures do not behave in quite the same way that homogeneous beds do, primarily due to variations in the angle of repose, ϕ, (not to be confused with the hillslope angle of repose mentioned above) of the grain above the bed. The angle of repose of a grain is the angle, relative to the plane of the bed, which its surface makes with the next grain immediately downstream of it. This angle can be considered to be a type of friction coefficient. It takes on a smaller value with increasing grain size because as a grain becomes larger relative to the bed roughness height, it protrudes more into the flow, resulting in a higher velocity contrast between the top and bottom of the grain, which in turn results in a proportionally larger fluid force. In the two-dimensional case (i.e., unidirectional fluid flow) the angle of repose can be expressed mathematically as:

$$\phi = \cos^{-1} \frac{D/_{ks} + z*}{D/_{ks} + 1}$$

where ϕ = angle of repose at which motion begins, D = grain diameter, k_s = bed roughness height, z* = the mean height of the bottom of the particle which is about to be set in motion. A lower value of ϕ reduces the value of τ_{*crit} by reducing the amount by which the grain must be rotated by the flow before becoming fully dislodged and entering bedload transport.

Wilcock et al. 2001 found through flume experimentation that gravel transport increases by multiple orders of magnitude with increasing sand content and constant flow strength, despite the fact that the relative proportion of gravel in the mixture was lower. Critical dimensionless shear stress therefore appears to be lowered, to 0.015 (a 62% decrease from the unisize Shields value of 0.06) in some cases, by the content of sand on the bed (Wilcock et al. 2001).

Wilcock & Kenworthy 2002 developed a model of the transport of mixtures of gravel and sand which explicitly took into account the two different size fractions in the bed and in transport, motivated by numerous observations of the difference in transport behavior of sediments as the percentage of sand on the bed surface and in the subsurface increases. As the content of sand on the surface, f_s, on the bed grows (f_s=1 for 100% sand), fewer grains in the large fraction are in contact with one another. This results in increased transport of gravel, due to a reduced angle of repose, reduced (or eliminated) friction between gravel grains, undercutting of the sand upstream of the gravel grain, and a smoother surface over which the gravel moves.

A dimensionless transport function was fitted to both field and laboratory observations:

$W_i^*=0.002\varphi^{7.5}$ for $\varphi<\varphi'$, and

$W_i^*=A(1-\frac{\chi}{\varphi^{0.25}})^{4.5}$ for $\varphi\geq\varphi'$

Where $\varphi = \tau/\tau_{ri}$ (τ_{ri} is a reference shear stress for sand or gravel which produces a reference value of W_r^*=0.002), φ' is the value of φ where the slopes of these two functions are equal, χ is the value of W_i^* at φ', and A is a fitted parameter.

An expression of critical dimensionless shear stress for each of the two size fractions of the form:

$$(\tau_{rs}{}^*)_0 = \alpha(\tau_{rg}{}^*)_0(\frac{D_g}{D_s})$$

is developed, where $(\tau_{rs}{}^*)_0$ and $(\tau_{rg}{}^*)_0$ are reference values of critical dimensionless shear stress when f_s=0, α is a constant, and D_s, D_g are diameters of sand and gravel grains, respectively. When these reference values are plotted against f_s as in figure X, the following exponential function was fitted to the curve:

$$\tau_{ri}{}^* = (\tau_{ri}{}^*)_1 + [(\tau_{ri}{}^*)_0 - (\tau_{ri}{}^*)_1]e^{-14f_s}$$

where the subscript of 1 indicates f_s=1. When f_s=1, the reference value for critical dimensionless shear stress for gravel, $(\tau_{rg}{}^*)_1$, takes a value of 0.011, although it comes close to this value at $f_s\cong$0.2, (see Figure 7) indicating a change in behavior from a clast-supported and a matrix-supported bed.

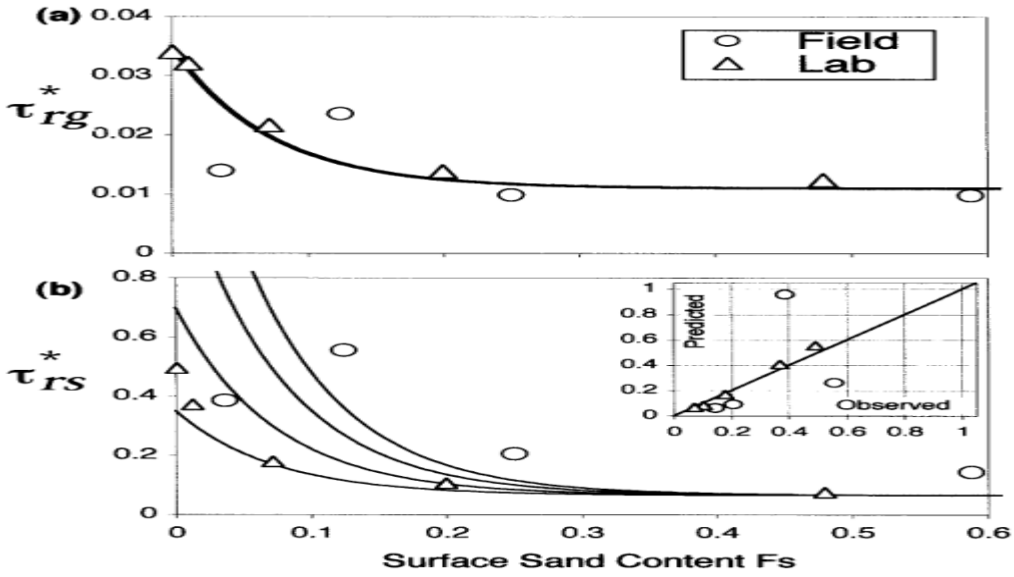

Figure 7. Calculated reference critical dimensionless shear stress values for different ratios of gravel to sand grain diameters. From left to right, these values are 10, 20, 35, and 50. From Wilcock & Kenworthy 2002.

While the true fraction of sand content on the bed surface can, in principle, be approximated from the SLI and MRI images, this is not necessary. Most of the cobbles on the surface are not in contact with one another, indicating a largely matrix-supported bed surface. The ratio Dg/Ds is also greater than 50, when considering the largest grain size of 20 cm and the mean size of 2 mm in the small fraction.

Previous application of sediment transport theory to Titan:

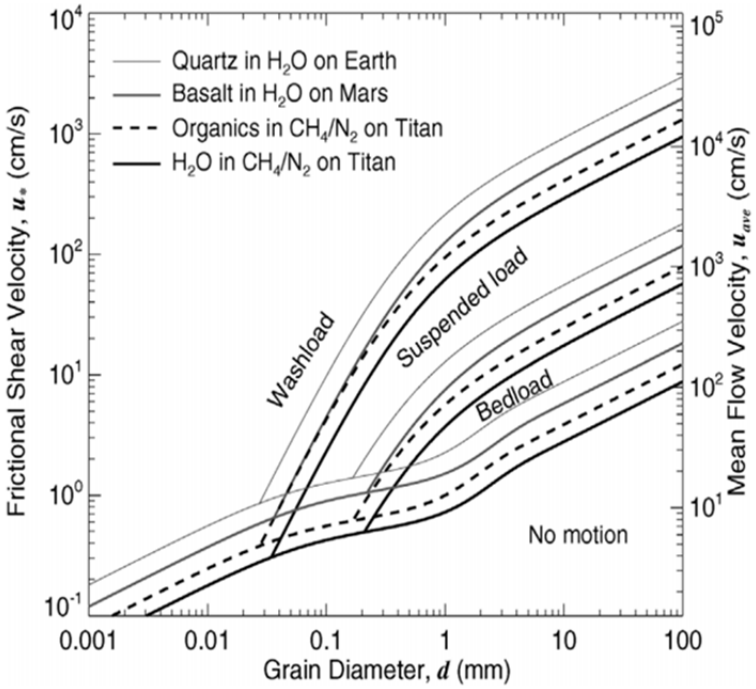

Figure 8. Theoretical thresholds of motion for sediments on Earth, Mars, and Titan.

Burr et al. 2006 derives theoretical initiation of motion and transport mode thresholds for basalt sediment on Mars, quartz sediment on Earth, and both water ice and organic sediment on Titan. They assumed a density of 1500 kg/m^3 for the organics based on previous work by other researchers. A threshold of motion curve was generated on a plot of particle diameter vs. fluid shear velocity (Figure 8), which showed that entrainment occurs at lower flow velocities on Titan than on Earth or Mars due to the (likely) lower density of Titan's sedimentary material and Titan's weaker surface

gravity (Burr et al. 2006). This is despite the much lower viscosity of liquid methane compared to liquid water. The study was limited to grain motion in the case of homogeneous grain size, a mechanically non-cohesive stream bed, pure methane liquid, and laminar Stokes grain settling velocities.

I propose the following hypothesis under the assumption that sediment transport theory for Earth processes, including the effects of heterogeneous particle mixtures on critical shear stress, can be applied to Titan.

Hypothesis: Sand transitions from suspended load to bed load near the deposition site, therefore, *there is a small number of fluid and sediment characteristics* that fit the observed grain sizes and critical dimensionless shear stress values.

Null Hypothesis: There is a *wide range of fluid and sediment characteristics that fit observed values*. Thus sediment transport theory does not help constrain fluid and sediment parameters on Titan.

KNOWN CONSTRAINTS ON SEDIMENT AND FLUID PROPERTIES:

Fluid viscosity and density:

The viscosity of pure liquid methane is 208 μPa-s at 94 K; its density is 454 kg/m^3 (Lorenz et al. 2010). In a study of the radar reflectivity of Titan's lakes, Lorenz et al. 2010 found that the high degree of smoothness observed on the liquid surfaces (i.e., the height of the waves generated by wind) was not consistent either with pure methane's low viscosity, or observed peak wind speeds of 1.5 – 2 m/s, adding support to the idea that the fluid which composes the lakes is in fact a mixture of multiple fluids. Nitrogen, ethane, propane, nitrile, and acetylene, among others, have all been proposed to be constituents of the mixture (Lorenz et al. 2010). Some of these compositions, especially those rich in propane or butane, have viscosities an order of magnitude higher than that of pure methane. Photochemical debris settles from Titan's atmosphere onto its surface; in lakes, this debris will likely have such a small settling velocity that they are effectively suspended in the liquid, resulting in an increase in the bulk viscosity (Lorenz et al. 2010).

Even though there is no explicit reason to believe that the polar lakes necessarily have the same composition as the equatorial precipitation/runoff, the assumption that the fluid is unlikely to be pure methane is still reasonable. I have therefore chosen to vary the fluid viscosity as an input parameter from 208 – 2000 μPa-s to account for a wide range of different possible fluid mixtures. The density of the fluid is also expected to vary for the same reasons as fluid viscosity. The boundary values of the fluid density will range between 454 kg/m^3, that of pure methane, to 800 kg/m^3, that of liquid nitrogen.

Sediment density:

Considering the active and extremely complex chemical environment of Titan's surface, the bedrock is unlikely to be composed of pure water ice. Evaporites formed by drying lakes, such as Ontario Lacus, may also be a common feature on Titan (Barnes et al. 2011). Areas known to be presently dry lakes have spectral properties which are different both from the surrounding terrain and from the channels through which liquid flows, prompting speculation that the lake-beds may be mantled in

material precipitated from the methane-ethane mixture in closed basins (Barnes et al. 2011). Solid mixtures of hydrocarbons and water ice, whether formed through evaporitic, sedimentary, or cryo-igneous process, are altogether more likely to be the norm. Regardless of the petrological processes involved, the densities of the rocks can deviate from that of water ice. Thus, the density of the grains is a parameter as well, and will be considered in the range of 500 – 1500 kg/m^3. The upper limit corresponds to the density of tholins material taken by Burr et al. 2006, and the lower limit is chosen to account for the potentially large degree of incorporation of lighter hydrocarbon material into the water-ice rocks.

MODEL:

Determination of particle fall velocity:

In order to determine the fall velocities of sediment particles, Dietrich 1982 derives a relationship between two quantities known as the dimensionless fall velocity, W_*, and the dimensionless grain diameter, D_*:

$$W_* = \frac{\rho w^3}{(\sigma-\rho)g\upsilon}$$

and $D_* = \frac{(\sigma-\rho)gD^3}{\rho\upsilon^2}$,

where ρ = fluid density, σ = particle density, w = fall velocity, g = gravitational acceleration, υ = μ/ρ = kinematic viscosity of the fluid, and d = grain diameter. A least-squares fit of the curve generated by plotting W_* as a function of D_* (Figure 9) yields the following polynomial (Dietrich 1982):

$$\log(W_*) = -3.76715 + 1.92944\log D_* - 0.09815(\log D_*)^{2.0} - 0.00575(\log D_*)^{3.0} + 0.00056(\log D_*)^{4.0}$$

These logarithms are expressed in base 10. Fixing values for each of the parameters ρ, σ, μ, and D, the value of D_* thus obtained is used in the above equation, which produces a value of W_* which is then solved for w. The particles here are approximated as spheres, an approximation often made in sediment transport mechanics for ease of calculation.

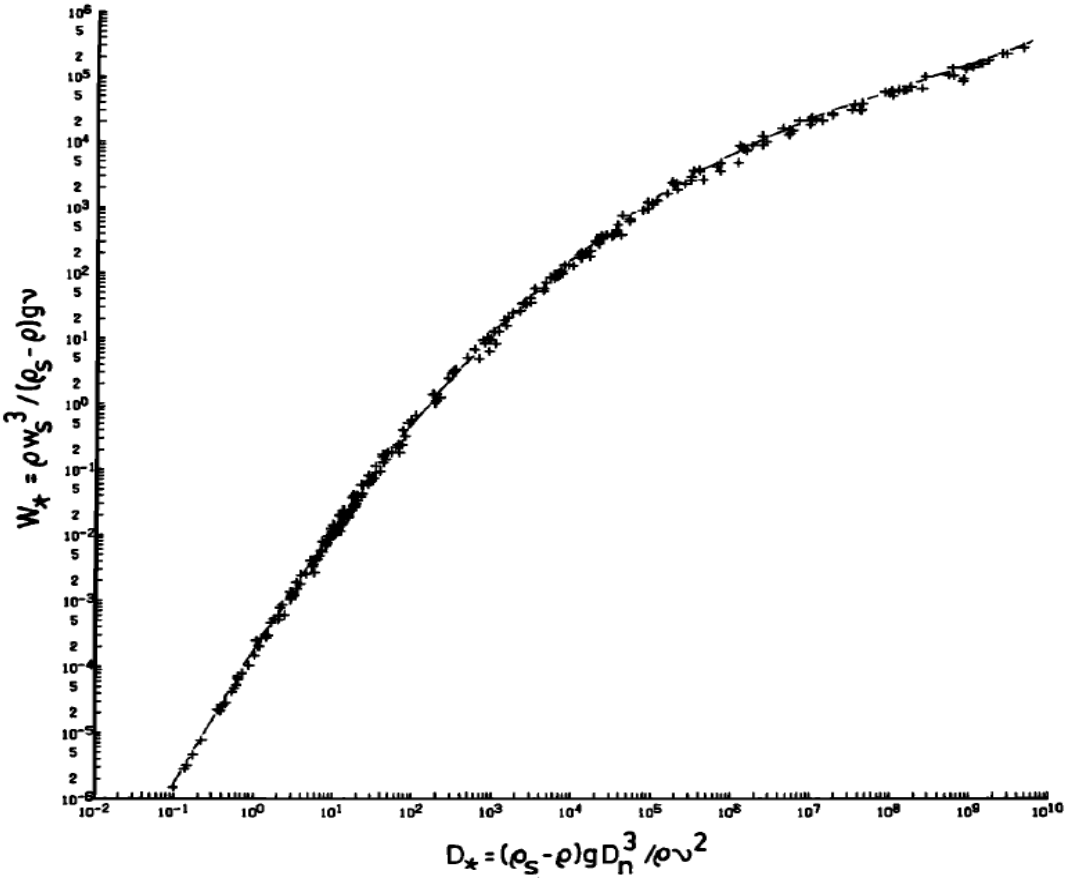

Figure 9: Dimensionless grain diameter plotted against dimensionless fall velocity. This plot is used to determine particle fall velocity, and incorporates properties of both the fluid and the particle (Dietrich 1982).

Determination of critical shear velocity:

The Rouse number is a dimensionless quantity which is used to describe the concentration of suspended sediment with height above the bed and the susceptibility of a grain to enter into suspension. It takes the form:

$$Z = \frac{w}{BkU_*}$$

where w is the settling velocity, B is a constant relating to eddy viscosity and eddy diffusivity (often taken to equal 1), and k = 0.41 is von Karman's constant, which relates to the logarithmic velocity profile of a turbulent fluid flow. U_* is the shear velocity, a quantity describing shear stress and fluid density in units of velocity. It is used in the "law of the wall", the same law from which von Karman's constant is derived, as a way of non-dimensionalizing the fluid velocity profile of a wall-bounded turbulent flow.

Determination of shear stress necessary to carry sediment in suspension:

Shear velocity is related to shear stress by the following equation

$U_* = \sqrt{\tau_s/\rho} = \sqrt{gdS}$

where τ_s = critical shear stress at that level in the flow at which suspension occurs, d = depth of flow and S = slope over which flow occurs. When Z = 1, U_*/w = Bk, the shear velocity is at a threshold value, above which the grain will enter into suspension. Solving for shear stress τ_s yields the minimum critical shear stress at a given height z in a flow of depth h required to transport the grain in suspension.

Determination of shear stress at channel bed:

Shear stress in an open-channel flow decreases linearly with height above the bed. So if the shear stress at one height is known in the fluid column, the shear stress at some other height can easily be extrapolated by constructing a scaling factor. While the actual depth of the flowing liquid cannot be directly constrained using this method, the relative height above the bed in the flow, above some arbitrarily small reference level can still be expressed mathematically as $\frac{h}{z}$ where h is the total depth of the flow, z is the depth in the flow in which suspension is occurring, measured *downward* from the liquid surface. When sediment is being deposited on a bed by a waning flow event, the fine material remains in suspension until it reaches a depth which is generally considered to be 1/20 of the total flow depth, or at z=0.95h. Therefore, if the shear stress τ_s at 1/20 of the height above the bed relative to the total flow depth is known, to determine the shear stress at the bed, the shear stress derived above, τ_s, is multiplied by the factor: $\frac{h}{0.95h} = 1.05$. The shear stress τ_{bed} at the bed is therefore 1.05 times that at height z.

Determination of maximum grain size moved at bed:

Finally, the maximum grain diameter which can be set in motion by this bed shear stress, D_b, can be calculated simply by rearranging the critical dimensionless shear stress equation after defining a value for τ_{*crit}:

$D_b = \frac{\tau_{bed}}{(\tau_{*crit})(\sigma-\rho)g}$

Of interest are the ranges of each parameter which provide the size distribution of the larger grains outlined by Keller et al. 2008.

<u>Model Description:</u>

The model consists of two components. The first is the process developed above, in which maximum bedload grain size is predicted from suspended load grain size through a series of calculations based on dimensionless numbers and basic sediment transport equations. The second component evaluates the most plausible solutions for each of the parameters which are compatible with both the observed grain size distribution and the specified ranges of each parameter. The model begins by specifying the value of the observed maximum grain size in the larger size fraction (20 cm), as well as a measure of uncertainty associated with this grain size.

Boundary values for each of the parameters are then defined. These are the boundary values stated above, namely: $2.08*10^{-4}$ Pa-s $\leq \mu \leq 2*10^{-3}$ Pa-s for viscosity; 456 kg/m^3 $\leq \rho_{fluid} \leq$ 800 kg/m^3 for fluid

density; and 500 kg/m^3 $\leq \rho_{sediment} \leq$ 1500 kg/m^3 for sediment density. A random value between minimum and maximum is then selected for each parameter by multiplying the difference between maximum and minimum by a random number between 0 and 1 and adding it to the minimum.

These values are then used in the calculation of a predicted value of maximum bedload transport size in the first function, and this value is then plugged into a Gaussian distribution which uses the observed grain size value (20 cm) as its mean, and the chosen grain-size step length as its standard deviation:

$$\mathrm{L} = -\frac{(Db_{pred} - Db_{obs})^2}{2{D_{std}}^2}$$

Where Db_{pred} is the predicted value from the randomly selected parameters, Db_{obs} is the observed grain size value, and Db_{std} is the assigned uncertainty in the grain size value. The mean, in this case, is at the top of the bell curve, so L at the given value is greater when the predicted value more closely matches the observed value.

A Markov chain Monte Carlo process has been used in this model, which utilizes a random walk through many iterations in order to generate a probability distribution of parameter values. A step length is chosen, which, when multiplied by a random number chosen from an ideal Gaussian distribution, is added to the new value of the parameter. Provided that this new value lies within the pre-defined boundaries, it will be used in the computation of another value of L. If this $L_{new} > L_{old}$, these new parameter values will be retained. If $L_{old} > L_{new}$, then the probability that the parameter values which generated L_{new} will be used in the next iteration is $P = e^{L_{new} - L_{old}}$, if P is greater than a randomly generated number between 0 and 1. This satisfies the Metropolis criterion, which uses a rule to alter the random walk from complete randomness to one which samples the probability distribution of interest with increasing frequency as the process is repeated. A large number of iterations of the above process must be performed in order to adequately sample the probability distribution. In this case, 10^{10} iterations were found to be required. After the program has performed half of the predetermined total number of steps, every thousandth value for each parameter is retained as an output value, and it is used in the histogram. This is because the model's outputs are not well realized early in the process – it helps to minimize superfluous outliers.

The final result is a set of three histograms of values of each of the three parameters plotted against the number of individual iterations for which that value as a solution. A peak in such a histogram corresponds to the value which is probable, given that set of bounding values. Conversely, if there is no peak, then all or most of the values have equal probability of fitting the solution, and there is thus a wide range of parameter values which can produce the grain size distribution observed at the landing site, confirming the null hypothesis.

Model Results:

Effect of step length choice:

The step lengths for each of the parameters are an important consideration as well. The "length" of a step in a random-walk process will influence how the parameter space is "covered" – depending on the size of the parameter space, remaining within the region of interest in this space can be less efficient with a longer step length, but mapping this region thoroughly can be less efficient with a shorter step length.

Rather than experiment with many different possible combinations of high step length for some parameters and low step length for others, I decided simply to run the model at long, moderate, and short step lengths for each parameter for each combination of grain size values. Three or four trials for each set of inputs were performed in order to obtain means and standard deviations, the results of which are displayed in Tables 1-3. Red text denotes questionable values taken from suboptimal peaks, which were not used in the calculations of means and standard deviations. Figures 10, 11, and 12 are examples of the effect of varying step length on the general forms of the plots. The qualities of the plots showed a slight improvement with shortened step length.

The standard deviations of the results given by the intermediate step lengths are even greater than those for the longest step length, contrary to expectation, but the standard deviations produced by the shortest step length do appear to be the smallest. This may be an artifact of the small sample size for each set of input values – however, time constraints prevented the generation of a sufficiently large number of plots to further investigate this issue.

Sensitivity of the model to grain size:

Sediment transport processes, especially suspension, are sensitive to grain size. Grain size input values were therefore varied to test the parameter sensitivity of the model. The maximum grain size of the coarse fraction is taken to be 20 cm, but values of 19 and 21 cm were used as well. Similarly, while the mean grain size of the fine suspended fraction is taken to be 2 mm, values of 1.9 and 2.1 mm were also used. There does not appear to be a correlation between divergence from the nominal grain size values and standard deviation of the sediment density values. Figures 13 - 16 illustrate the diversity of values produced by the same sets of parameters, as well as the same values being produced by both reducing and increasing grain sizes.

TABLE 1: Long step lengths. 0.0001 Pa-s for viscosity, 75kg/m^3 for densities.

	Sediment density:			step lengths							
				densities	viscosity	trial #					
Plot #	Db (cm)	Ds (mm)	Db_std	(kg/m^3)	(pa-s)	1	2	3	4	Mean	Std
1	19	1.9	0.01	75	1.00E-04	735	768	709		737.3	29.6
2	19	2	0.01	75	1.00E-04	725	768	735		742.6	22.5
3	19	2.1	0.01	75	1.00E-04	715	755		735	735	20
4	20	1.9	0.01	75	1.00E-04	745	815	804	734	761	40.1
5	20	2	0.01	75	1.00E-04	735	735	777		749	24.2
6	20	2.1	0.01	75	1.00E-04	725	745	735		735	10
7	21	1.9	0.01	75	1.00E-04	772	735	737		748	20.8
8	21	2	0.01	75	1.00E-04	796	745	735		758.6	32.7
9	21	2.1	0.01	75	1.00E-04	735	782	735		750.6	27.1

TABLE 2: Intermediate step lengths. 0.00005 Pa-s for viscosity, 50 kg/m^3 for densities.

	Sediment density:			step lengths							
				densities	viscosity	trial #					
Plot #	Db (cm)	Ds (mm)	Db_std	(kg/m^3)	(pa-s)	1	2	3	4	Mean	Std
10	19	1.9	0.001	50	5.00E-05	780	745	786		770.3	22.1
11	19	2	0.001	50	5.00E-05	735	633	745	735	704.3	52.9
12	19	2.1	0.001	50	5.00E-05	744	752	725	735	740.3	11.6
13	20	1.9	0.001	50	5.00E-05	800	735	687		740.6	56.7
14	20	2	0.001	50	5.00E-05		732	742	654	709.3	48.2
15	20	2.1	0.001	50	5.00E-05	712	608	758		692.6	76.8
16	21	1.9	0.001	50	5.00E-05	735	790	734		753	32
17	21	2	0.001	50	5.00E-05		745	735	755	745	10
18	21	2.1	0.001	50	5.00E-05	745	725	738		736	10

TABLE 3: Short step lengths. 0.00001 Pa-s for viscosity, 25 kg/m^3 for densities.

	Sediment density:			step lengths							
				densities	viscosity	trial #					
Plot #	Db (cm)	Ds (mm)	Db_std	(kg/m^3)	(pa-s)	1	2	3	4	Mean	Std
19	19	1.9	0.0001	25	1.00E-05	735	785	752		757.3	25.4
20	19	2	0.0001	25	1.00E-05	735	725	697	735	723	18
21	19	2.1	0.0001	25	1.00E-05	725	731		731	729	3.5
22	20	1.9	0.0001	25	1.00E-05	755		735	735	741.6	11.5
23	20	2	0.0001	25	1.00E-05	796	735	755		762	31.1
24	20	2.1	0.0001	25	1.00E-05	725		725	725	725	0
25	21	1.9	0.0001	25	1.00E-05	735	735	775	735	735	0
26	21	2	0.0001	25	1.00E-05	735	725	763		741	19.7
27	21	2.1	0.0001	25	1.00E-05		765	735	749	749.6	15

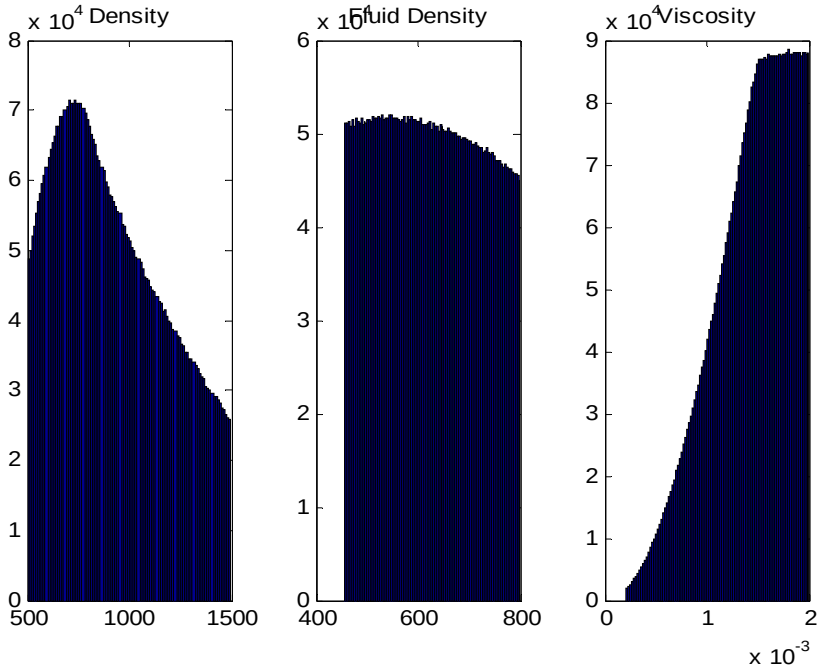

Figure 10. An example of a plot where Db = 20 cm, Ds = 2 mm and longest step length used. Note the significantly less optimal peak for fluid density. The majority of fluid density peaks belong to this category.

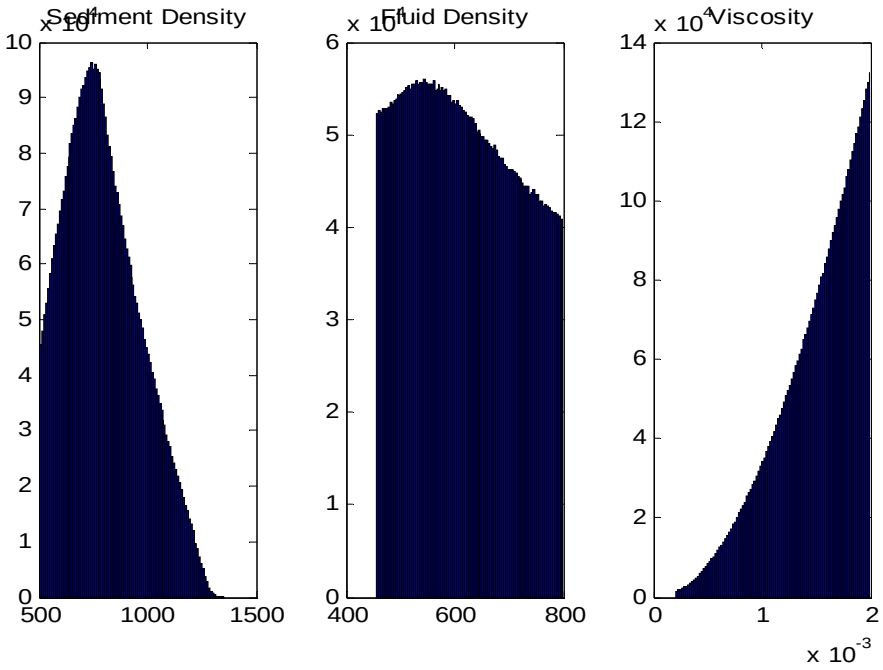

Figure 11. An example histogram where Db = 20 cm and Ds = 2 mm and the intermediate step length was used.

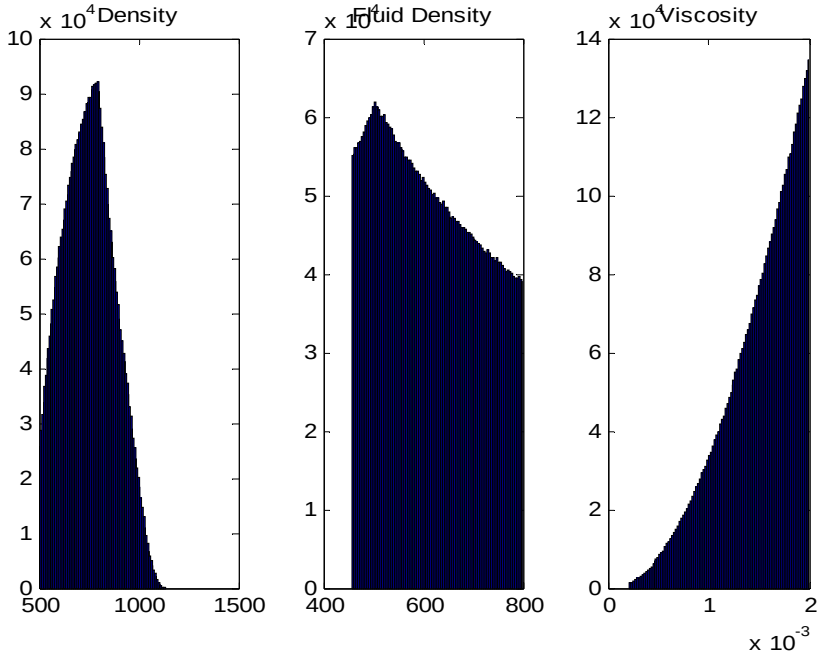

Figure 12. An example histogram plot where Db = 20 cm and Ds = 2 mm, and the shortest step length was used. The fluid density peak is neatly defined in this plot, with a peak bin center at 502 kg/m^3.

Sediment density:

The model provided the best constraints on the density of the sediments. The sediment densities were in the range of 700 – 800 kg/m^3, with a modal value of 735 kg/m^3. The histogram peaks were much more sharply defined for the sediment density than for the fluid density. The distribution of densities was very similar across nearly every run of the model, as seen in figures XXX

Fluid Density:

Less than half of the histograms showed good peaks like the one shown in Figure 12, but rather displayed broad, shallow peaks like those shown in Figure 10. Nonetheless, the sharper peaks, when present, lie mostly within the range of 500 – 550 kg/m^3.

Fluid Viscosity:

No viscosity peak was produced in any iteration of the model. Instead, the values in each histogram either increased steadily until the upper boundary was reached, or increased as viscosity increased until reaching a value which remained constant as viscosity increased further, seemingly indicating that fluids of high viscosities are more capable of transporting the sediment.

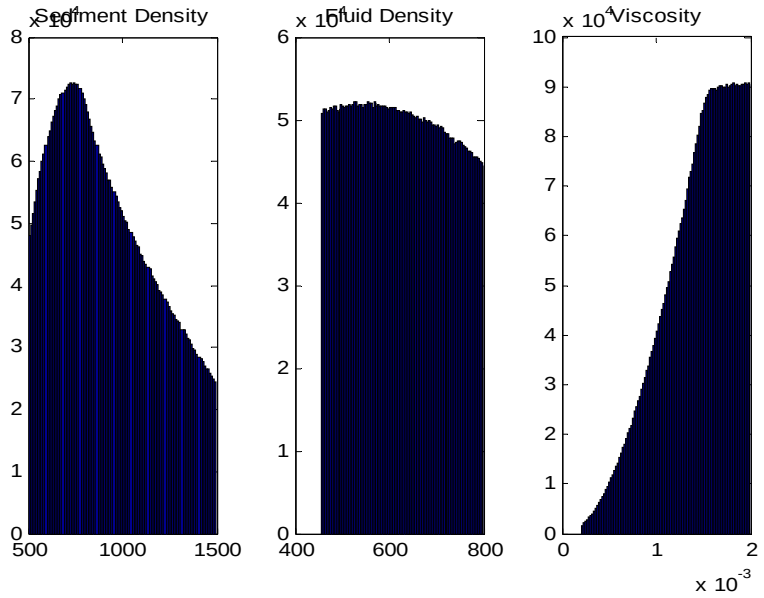

Figure 13. Both Db and Ds were reduced for this plot to values of 19 cm and 1.9 mm, respectively. The sediment density peak lies at the modal value of 735 kg/m^3.

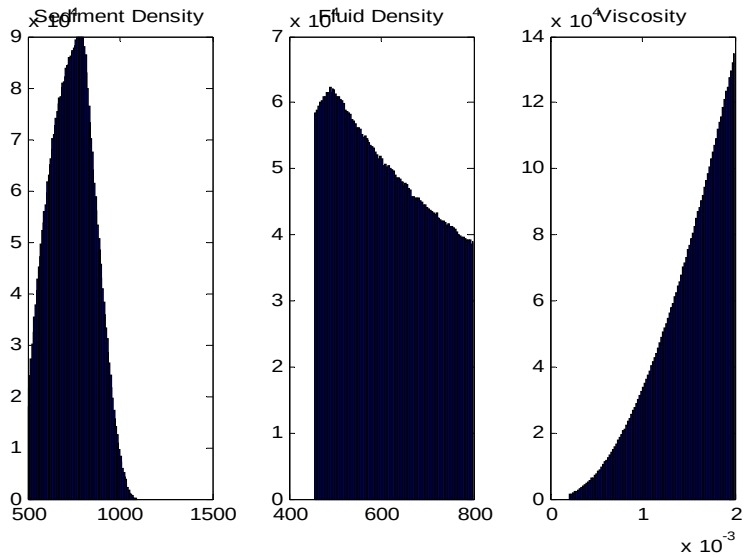

Figure 14. The same set of parameter values as Figure 13 above, but sediment density shows a peak at 785 kg/m^3 instead.

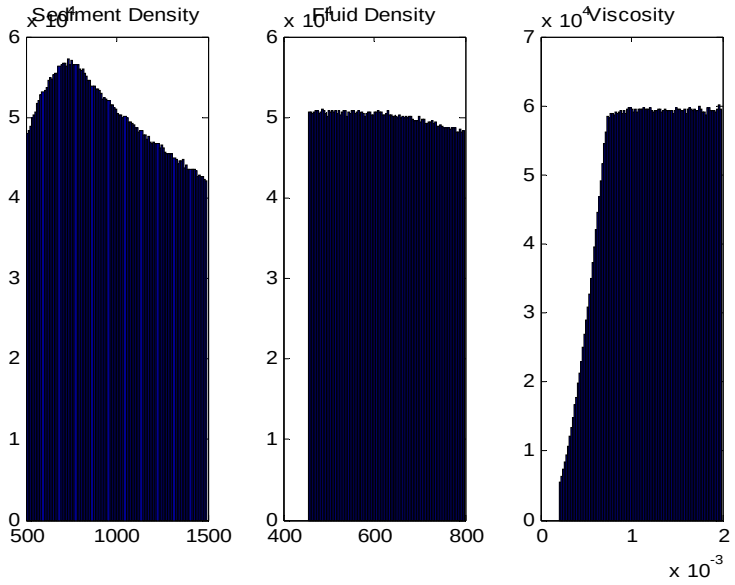

Figure 15. In this plot, Db and Ds were both increased to values of 21 cm and 2.1 mm, respectively. This set of values also produced the modal value of 735 kg/m^3 for sediment density.

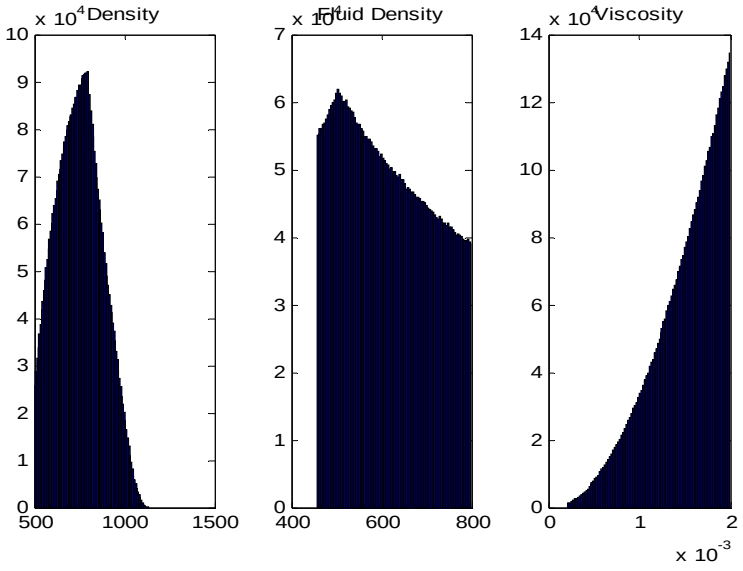

Figure 16. The nominal values of grain size also produced different values of sediment density – here the peak lies at 796 kg/m^3.

Effect of restricting sediment density boundary values:

The choice of boundary values may also affect the outcome, and therefore should also be varied. Since the majority of sediment density values lay within the interval of 700 – 800 kg/m^3, using new boundary values which are closer to this range of values may serve to provide further constraints to the value which is most likely to be true. The initial range was 500 – 1500 kg/m^3 – this was restricted to 500 – 1000 kg/m^3, and then restricted again to 650 – 850 kg/m^3. Narrowing the range of sediment density boundary values did not appear to provide more significant constraints on the values of sediment density produced – in fact, while the mean remained mostly unaffected, the standard deviation actually increased, as illustrated in Table 4 and Figures 17 – 20.

Table 4: Effects of narrowing the range of sediment density values on model result

Window narrowings:						
	trial #					
Boundary values:	1	2	3	4	mean	std
500-1000	737	707	737	788	742.25	33.6
650-850	779	779	687	779	756	46

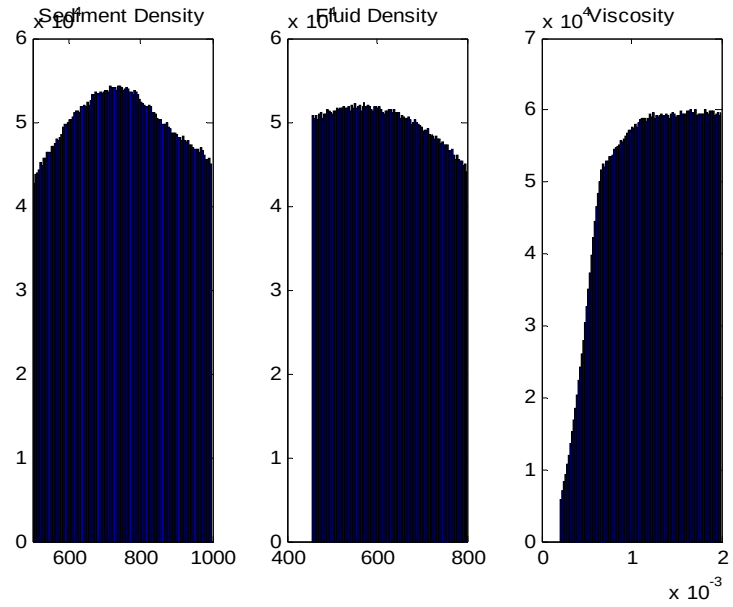

Figure 17. Narrowing of the boundary values of sediment density to 500 – 1000 kg/m^3. Db = 20 cm and Ds = 2 mm, shortest step length. The sediment density peak lies at 737 kg/m^3.

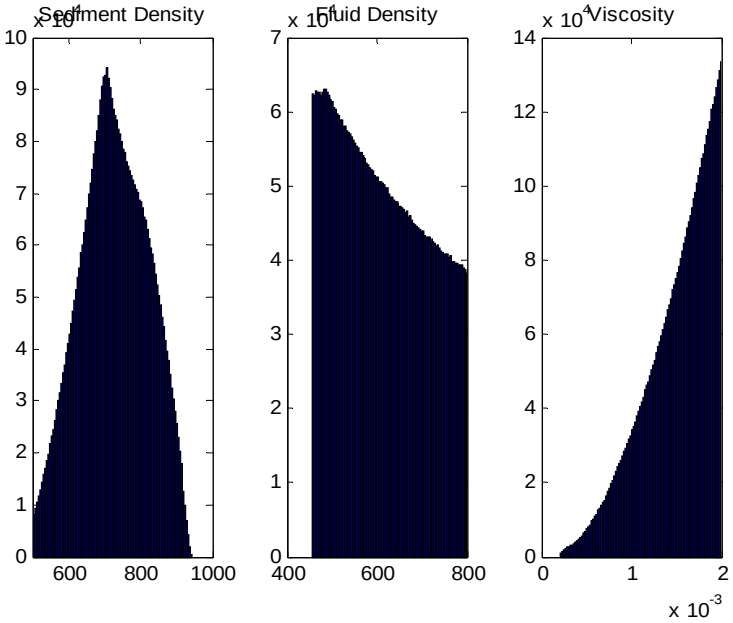

Figure 18. The same narrowing of boundary values, and the same grain sizes, as in Figure 17. The sediment density peak here lies at 707 kg/m^3.

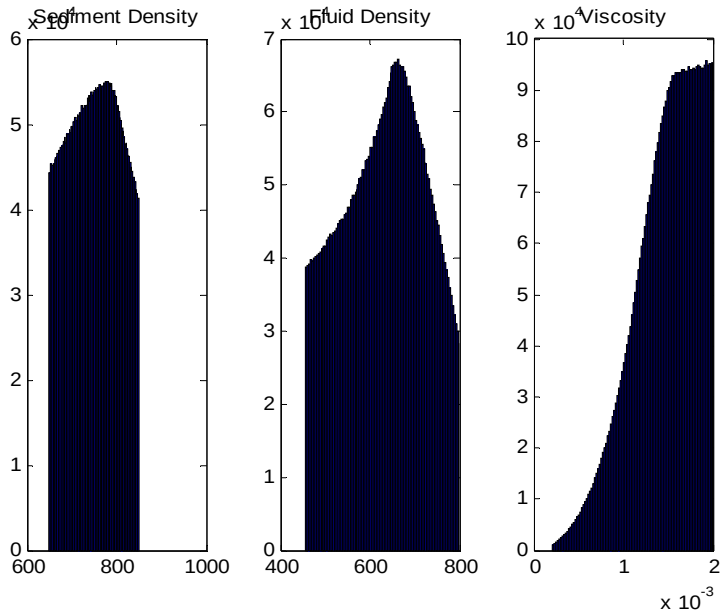

Figure 19. Narrowing of the boundary values of sediment density to 650 – 850 kg/m^3. Db = 20 cm and Ds = 2 mm, shortest step length. The sediment density peak lies at 779 kg/m^3.

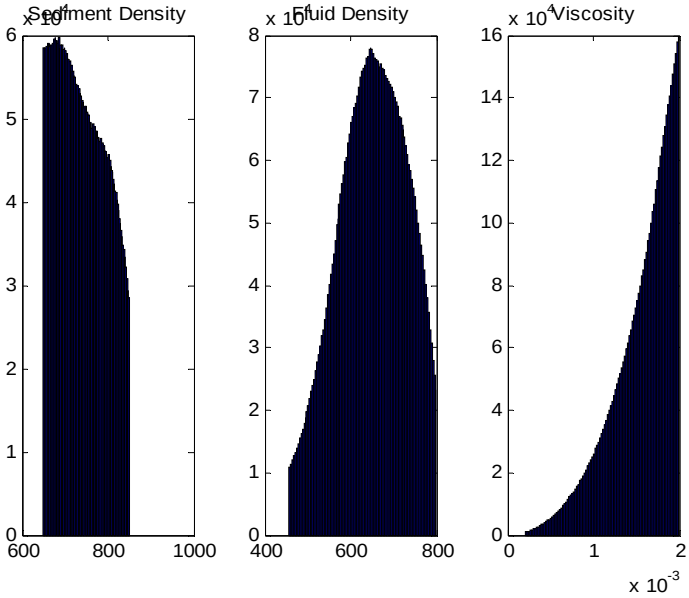

Figure 20. The same narrowing of boundary values, and the same grain sizes, as in Figure 15. The sediment density peak here lies at 687 kg/m^3.

Discussion:

Constraints on sediment density:

The density of the sediment was the only parameter of the three which was well-constrained. The density of the sediment was significantly lower than that of water ice, suggesting that it contains a minimal amount of silicate material, which is generally denser than water ice by a factor of 2 - 3. Hydrocarbon compounds, such as heavier alkanes like propane and butane, almost certainly permeate into the water ice surface rock and remain as evaporites, reducing the rock's bulk density.

The fall velocity of a particle in a fluid is sensitive to particle size. The only information available on the grain sizes of the smaller fraction comes from experimental duplication of the signal sent from the penetrometer. This introduces a degree of uncertainty which may skew the results obtained toward a higher sediment density for a smaller grain size, or vice versa. This may serve as an explanation for the fact that variation of grain sizes, especially the size of the grain traveling in suspension, as input parameters, can produce density values which lie within the reasonably confined range of 700 – 800 kg/m^3 (and even seem to produce a modal value of 735 kg/m^3), but cannot unambiguously be confined within that range.

Constraints on fluid parameters:

Lorenz et al. 2010 note that the aerosol particles which continually precipitate out of Titan's atmosphere will settle in bodies of standing fluid. This particulate matter has settling velocities on the order of centimeters per year, and thus contributes greatly, by potentially an order of magnitude, to the bulk viscosity of the liquid. However, the liquid in the polar lakes does not necessarily have the same physical properties as the liquid which flows as runoff in equatorial channels shortly after being precipitated from the atmosphere. The lakes are of large areal extent and unknown age, and hence have had an unknown amount of time to accumulate atmospheric detritus through seasonal evaporation. The rain, however, although unlikely to be free from all particulate matter, is likely to be "cleaner", due to its small droplet size and comparatively far shorter residence time in the atmosphere.

The viscosities of stream flows on Earth can vary by orders of magnitude, even approaching the behavior of visco-plastic substances in the case of debris flows, depending on the concentration of suspended sediment (Pierson & Scott 1985). However, debris flows tend to have a much wider range of grain sizes, and do not produce bimodal size distributions such as the one at the Huygens landing site. Sediment-laden flows can exhibit a variety of rheological behaviors. According to Pierson and Scott 1985 in their study of the rheological development of a lahar flow as it became progressively diluted with water, a flow is hyperconcentrated when it has reached a sediment concentration of 37% by volume. If the flow which deposited the sediments at the Huygens landing site is indeed hyperconcentrated, it has a significantly higher viscosity than flows with a lower sediment concentration, but how this viscosity varies with concentration of fine water ice-based sediment in the exotic hydrocarbon fluid under consideration is unknown. The density of the fluid suffers from a similar ambiguity, in that the bulk density of the fluid-sediment mixture increases as deposition progresses as well. The density of the sediment particles, however, does not change as they are entrained in a fluid flow, providing one

potential explanation for the generally good constraints for sediment density compared to the other parameters.

Implications of sediment and fluid densities:

If a range of fluid density of 500 – 550 kg/m^3 can be reliably inferred from this model's behavior, then the density difference between the fluid and the sediment is much smaller, at roughly 200 – 300 kg/m^3, on Titan in comparison to Earth, where the commonly used density difference between water and quartz of 1650 kg/m^3. This would mean that critical dimensionless shear stress is much easier to achieve, since the density difference term is in the denominator – lower flow depths or shallower slopes than on Earth are suitable for moving sediment on Titan. A potentially interesting consequence of this is that fluvial erosion rates on Titan may be comparable to those on Earth even if actual fluvially significant events are far less frequent.

CONCLUSION:

The sediment transport mechanics-based method devised in this paper is useful for constraining the density of the sedimentary material, and, to a lesser extent, the density of the transporting fluid, at the Huygens landing site. The modal value of sediment density is 735 kg/m^3, and the overall range of values lies within 700 – 800 kg/m^3, indicating a predominantly water ice composition mixed with alkaniferous material and a lack of silicates. The fluid density is less strongly constrained, but the most probable values are in the 500 – 550 kg/m^3 range. The null hypothesis has been confirmed, however, for the viscosity of the fluid, perhaps due to increases in viscosity caused by hyperconcentration of suspended material in the flow during the late stages of fluvial deposition. If the predictions of fluid and sediment density made by this model are accurate, then a geomorphologically relevant consequence of smaller density differences when compared to Earth is that sediment transport occurs much more easily on Titan than on Earth.

Acknowledgements: I would like to acknowledge Dr. Karen Prestegaard, my thesis advisor, as well as Dr. Vedran Lekic for his indispensable assistance in developing the MATLAB code used in the model.

References:

Atkinson, K.R. et al., 2010, Penetrometry of granular and moist planetary surface materials: Application to the Huygens landing site on Titan: Icarus, v. 210, pp. 843-851.

Barnes, J.W. et al. 2011, Organic sedimentary deposits in Titan's dry lakebeds: probable evaporite: Icarus, v. 216, pp. 136-140.

Burr, D.M. et al., 2006, Sediment transport by liquid surficial flow: Application to Titan: Icarus, v. 181, pp. 235-242.

Burr, D.M. et al. 2012, Fluvial features on Titan: insights from morphology and modeling: Geological Society of America Bulletin, published online, doi: 10.1130/B30612.1.

Burr, D.M. et al. 2013, Morphology of fluvial networks on Titan: Evidence for structural control: Icarus, v, 226, pp. 742-759.

Dietrich, W.E., 1982, Settling velocity of natural particles: Water Resources Research, v. 18, pp. 1615-1626.

Keller, H.U., et al., 2008, The properties of Titan's surface at the Huygens landing site from DISR observations: Planetary and Space Science, v. 56, pp. 728-752

Lorenz, R. D., et al. 2010, Threshold of wave generation on Titan's lakes and seas: Effect of viscosity and implications for Cassini observations: Icarus, v. 207, pp. 932-937.

Owen, T., 1982, The composition and origin of Titan's atmosphere: Planetary and Space Science, v. 30, pp. 833-838.

Perron, J.T., et al., 2006, Valley formation and methane precipitation rates on Titan: Journal of Geophysical Research, v. 111, E11001, doi: 10.1029/2005JE002602

Pierson, C.P. and Scott, K.M., 1985, Downstream dilution of a lahar: transition from debris flow to hyperconcentrated streamflow: Water Resources Research, v. 21, pp. 1511-1524.

Soderblom, L.A., et al., 2007, Topography and geomorphology of the Huygens landing site on Titan: Planetary and Space Science, v. 55, pp. 2015-2024.

Tarantola, A., 2005, Inverse Problem Theory: Society for Industrial and Applied Mathematics

Tomasko, M.G. et al., 2005, Rain, winds and haze during the Huygens probe's descent to Titan's surface: Nature, v. 438, pp. 765-778.

Turtle, E.P., et al., 2011, Rapid and extensive surface changes near Titan's equator: Evidence of April showers: Science, v. 331, pp. 1414-1416.

Wiberg, P.L. and Smith, J.D., 1987, Calculations of the critical shear stress for motion of uniform and heterogeneous sediments: Water Resources Research, v. 23, pp. 1471-1480.

Wilcock, P.R. & Kenworthy, S.T., A two-fraction model for the transport of sand/gravel mixtures: Water Resources Research, v. 38, pp. 1194-1205.

Wilcock, P.R. et al., 2001, Experimental study of the transport of mixed sand and gravel: Water Resources Research, v. 37, pp. 3349-3358.

APPENDIX: MATLAB code used for the model

```
function[rhosed_out,rhofluid_out,visc_out] = infer_values_of_parameters()
% Markov Chain Monte Carlo with the Metropolis Algorithm...
% Explore values of rhosed, rhofluid, visc, T_starcrit across a range of
% possible values, and then see which sets of values are compatible with
% the observed Db_obs.
Db_obs=0.2;
% We first have to decide what is "close enough" --> specify an uncertainty
% for Db_obs:
Db_obs_std = .0001; % Same units as Db_obs. ALL UNITS ARE SI.

% Find a starting value for all parameters
% Set minimum and maximum values for rhosed, rhofluid, visc and relative
% height. We will choose random numbers between min_rhosed and max_rhosed and
march
% in random increments of rhosed_std (the "uncertainty")
min_rhosed = 500;
max_rhosed = 1500;
rhosed = rand(1)*(max_rhosed-min_rhosed) + min_rhosed;
rhosed_std = 25;

min_rhofluid = 456;
max_rhofluid=800;
rhofluid=rand(1)*(max_rhofluid-min_rhofluid) + min_rhofluid;
rhofluid_std=25;

min_visc = 2.08e-4;
max_visc= 2e-3;
visc=rand(1)*(max_visc-min_visc)+min_visc;
visc_std=1e-5;

% Calculate a starting "probabiliy" of this being the "right" set of
% parameter values...
[Db_pred] = predict_D_bed(rhosed,rhofluid,visc,z);
Likl = -0.5*(((Db_pred-Db_obs)^2)/(Db_obs_std^2));
Nsteps = 1e10;
nn = 0; % Counter for models in the ensemble
for j = 1:Nsteps
    % Make a random step....
    rhosed_new = rhosed + rhosed_std*randn(1);
    rhofluid_new=rhofluid+rhofluid_std*randn(1);
    visc_new=visc+visc_std*randn(1);
%     z_new=z+z_std*randn(1);
    if(rhosed_new>min_rhosed && rhosed_new<max_rhosed && ...
       rhofluid_new>min_rhofluid && rhofluid_new<max_rhofluid &&...
       visc_new>min_visc && visc_new<max_visc)
        % i.e. if they fall within the desired intervals
          % Calculate new "probabiliy" of this being the "right" set of
          % parameter values...
        [Db_pred] = predict_D_bed(rhosed_new,rhofluid_new,visc_new,z);
        Likl_new = -0.5*(((Db_pred-Db_obs)^2)/(Db_obs_std^2));

 % METROPOLIS CRITERION
    if(Likl_new>Likl)
        rhosed = rhosed_new;
```

```
        rhofluid=rhofluid_new;
        visc=visc_new;
      %  z=z_new;
    else
        % Choose the new value (rhosed_new) with a certain probability....
        Prob_accept = exp(Likl_new-Likl);
        if(Prob_accept>rand)
            rhosed = rhosed_new;
            rhofluid=rhofluid_new;
            visc=visc_new;
        %    z=z_new;
        end
    end
    end
    if(j>Nsteps/2 && mod(j,1000)==0)
        nn = nn + 1;
        rhosed_out(nn) = rhosed;
        rhofluid_out(nn) = rhofluid;
        visc_out(nn) = visc;
     %   z_out(nn) = z;
    end
end

figure; subplot(1,3,1); hist(rhosed_out,100); title('Sediment Density');
subplot(1,3,2); hist(rhofluid_out,100); title('Fluid Density');
subplot(1,3,3); hist(visc_out,100); title('Viscosity');

end

function[Dbed] = predict_D_bed(rhosed,rhofluid,visc,z)
%suspended grain size
Ds=0.002;
%relative height
z=0.95;
%von karman's constant
k=0.41;
%critical dimensionless shear stress
T_starcrit=0.01;
%gravity. constant.
g=1.35;

%dimensionless grain diameter number
Dstar=(rhosed-rhofluid)*rhofluid*Ds^3/visc^2;
%conversion to dimensionless fall velocity
WW=-3.76715+1.92944*log10(Dstar)-0.09815*(log10(Dstar))^2-
0.00575*(log10(Dstar))^3+0.00056*(log10(Dstar))^4;
%fall velocity
Vfall=(10^WW*(rhosed-rhofluid)*g*visc/rhofluid^2)^(1/3);
%shear stress above bed
T_suspcrit=Vfall^2*rhofluid/k^2;
%shear stress at bed
T_bedcrit=T_suspcrit/z;
%grain diameter at bed
Dbed=T_bedcrit/(T_starcrit*(rhosed-rhofluid)*g);

end
```

I pledge on my honor that I have not given or received any unauthorized assistance on this assignment/ examination.

_____